

Iterative Inverse Design Method with AUSM+-Up Scheme Implemented on Unstructured Grids

S. Ganesh* and B. V. S. S. Prasad†

Indian Institute of Technology, Madras, Chennai 600 036, India

DOI: 10.2514/1.B34216

An iterative inverse design method is developed for obtaining the blade geometry that corresponds to the required pressure distribution. AUSM⁺-up scheme is used for flux computation and implemented on finite volume unstructured grid. The blade geometry is modified after certain iterations, and the spring analogy is used for mesh deformation after each modification. The robustness of the method is determined by verifying that the final blade geometry is independent of the initial choice of the blade profile. Results for a compressor cascade are presented in this paper.

Nomenclature

a	= speed of sound, m s^{-1}
C_p	= coefficient of pressure
E	= internal energy, kJ
F	= force, N
H	= enthalpy, kJ
l	= unit normal vector of an edge
M	= Mach number
p	= pressure, Pa
p_o	= stagnation pressure, Pa
s	= curvilinear coordinate, m
T	= static temperature, K
T_o	= stagnation temperature, K
t	= time step, s
u	= velocity in x direction, m s^{-1}
V	= absolute velocity, m s^{-1}
v	= velocity in y direction, m s^{-1}
x, y	= Cartesian coordinate, m
α	= flow angle, deg
β	= stagger angle, deg
γ	= specific heat ratio
ζ	= spring stiffness, m^{-1}
ρ	= density, kg m^{-3}
Ω	= cell volume, m^3

Subscripts

i	= edge of a control volume
L	= Left control volume of an edge
n	= normal component
p, q, t, s	= node indices
R	= Right control volume of an edge
t	= tangential component
x	= x component
y	= y component
is	= isentropic

Superscripts

$iter$	= design iteration
k	= iteration count
n	= time step

I. Introduction

IN THE design of two-dimensional turbomachinery blade sections, two fundamental methodologies are generally followed: 1) direct approach and 2) inverse approach. In the direct method, the blade geometry is specified and the resulting aerodynamic performance is calculated. In the inverse design methods, the blade geometry is determined for a prescribed function, say a pressure distribution. A design based on the direct approach requires not only the prior knowledge and expertise of an aerodynamicist, but demands significant design space. On the other hand, as the inverse design methodologies require only a specified function of the chosen performance parameter, less expertise is adequate. These inverse methods can be broadly categorized based on factors such as flow regime, blade modification methodology, design variables, solution methodology and the like. The most commonly used inverse design condition is to specify either of the following: 1) individual static pressure distributions on the suction and pressure surfaces [1–4]; 2) combination of static pressure loading (difference in surface static pressure between the upper and lower surfaces of the blade) along with the thickness distribution [5–8]. The common aspect of both the approaches is to start from an initially guessed geometry and to compute the flowfield by a direct solver (DS). However, the methods differ in the application of boundary conditions and the subsequent geometry modification. In the former case, the classical slip condition (no normal velocity component) is replaced by the permeable-wall boundary condition (nonzero normal velocity component) and by calculating the unknowns on the blade wall with the compatibility relations. The blade geometry is then modified to obtain the imposed pressure distribution by using the estimated velocity field. However, in the second method, both tangency and imposed pressure jump are satisfied by enforcing the constraints on the y component of velocity and static pressure along the blade surface. The blade camber line is modified using the updated blade velocity and adding the imposed blade-thickness distribution to it. In the present work, the first method of the prescribed pressure distribution (PPD) along the blade surface is preferred because of its simplicity and robustness, as the thickness distribution need not be brought in.

Apart from the initially guessed geometry, the inverse design method involves the integration of either Euler or Navier-Stokes equations, which was termed as a direct solver. The unsteady forms of these equations are hyperbolic with respect to the independent time variable. Most of the current finite-volume-based inverse design

Received 20 December 2010; revision received 6 August 2011; accepted for publication 17 August 2011. Copyright © 2011 by the American Institute of Aeronautics and Astronautics, Inc. All rights reserved. Copies of this paper may be made for personal or internal use, on condition that the copier pay the \$10.00 per-copy fee to the Copyright Clearance Center, Inc., 222 Rosewood Drive, Danvers, MA 01923; include the code 0748-4658/12 and \$10.00 in correspondence with the CCC.

*Research Scholar, Thermal Turbomachines Laboratory, Department of Mechanical Engineering.

†Professor, Thermal Turbomachines Laboratory, Department of Mechanical Engineering.

procedures use the time-marching methods to preserve this hyperbolic nature during the calculation at all regimes. These algorithms differ mainly in the application of flux discretization schemes. For example, the upwind van Leer's flux-splitting scheme in [1,2,9], and the central difference scheme with artificial dissipation in [3–8] were used.

In the present work, the time-dependent system of compressible Euler equations is considered for the inverse design method. It is well known [10] that the traditional central or upwind schemes for flux computation yield inaccurate solution as the flow speed approaches zero. These inaccuracies are due to the incorrect scaling of dissipation term as $M \rightarrow 0$. It is shown in [11] that numerical results shows excessive and undesirable numerical dissipation due to the scaling by speed of sound.

Liou and Edwards [12] employed AUSM family of schemes with a new and interesting concept called numerical speed of sound, suitable for low-Mach-number flows. A common speed of sound in the calculation of interfacial fluxes is used so that the constraints of zero mass flux in the region of $M = 0$ are exactly satisfied. Further, the speed of sound is rescaled by a factor that is a function of local and reference Mach numbers. These Mach numbers are determined from the preconditioning of the Euler equations, as suggested by Weiss and Smith [13]. As an extension to the above idea and for the sake of simplicity, the scaling factor, which is only a function of reference Mach number, has been introduced in the AUSM⁺-up method. This method is thus found to be one of the best developed for finite-volume-based Euler codes and has shown its efficacy on structured grids [14].

However, implementation of AUSM⁺-up scheme on the structured grid in turbomachinery passages increases meshing complexity as it involves making block structures. Further, highly curved leading edges of the blade can be easily represented using unstructured grids. It is therefore proposed in the present paper to implement the AUSM⁺-up scheme on unstructured grids. Moreover, it has been noticed that AUSM⁺-up has been applied hitherto only for direct solvers [15] and not for inverse solvers, which require additional efforts for implementing the compatibility (with permeable-wall boundary) conditions on unstructured grids. The robustness of the method is also tested by carrying out the inverse design corresponding to a given pressure distribution from three different initial profiles.

II. General Methodology

The general methodology of the iterative inverse design starts with the DS of Euler equations for a presupposed geometric configuration, as shown schematically in the flowchart in Fig. 1. In other words, the initial (iter = 1) values of the calculated pressure distribution (CPD) is obtained from the inviscid flowfield for the assumed geometry by using the DS. For the purpose of modification of the geometry, the guessed boundary is replaced with a permeable boundary. To obtain the primitive variables on this boundary, another Euler solver [termed inverse solver (IS)] is used by replacing the classical slip condition by the compatibility relations. Note that if the normal velocity is positive, three eigenvalues of the Jacobian matrix become positive and one boundary condition is needed. However, if the normal velocity is negative, three eigenvalues become negative, and hence three boundary conditions are to be specified. The difference between the values of CPD and PPD are used to evaluate the normal velocity across the permeable wall. The time-marching computations are carried out until convergence (continuity of $1.e-5$ and momentum of $1.e-4$) is reached to obtain the PPD. However, this convergence criterion with respect to PPD does not ensure the desired (zero) normal velocity on the wall by the inverse solver. This nonzero normal velocity and the value of tangential velocity on the blade surface are used to displace the wall boundary nodes, by means of streamline mode, which is in turn used for geometry modification. This procedure is repeated until a prescribed accuracy of 0.005 is achieved in the CPD and also the rms value of the normal velocity distribution on the blade in the IS does not exceed 7%.

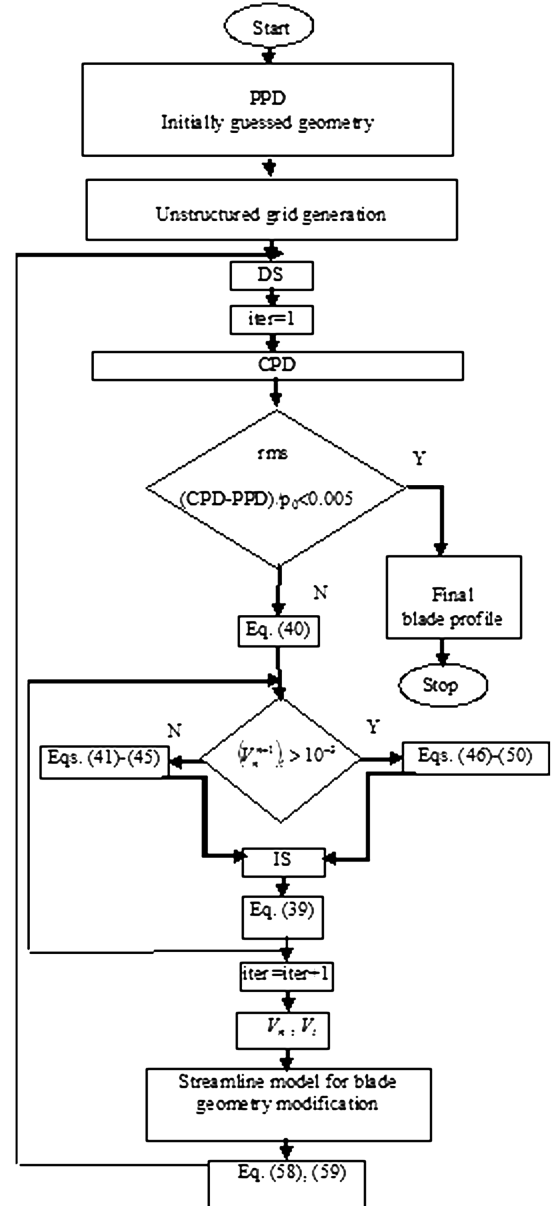


Fig. 1 Flowchart indicating iterative inverse procedure with embedded Euler code.

The four important steps that are specific contributions to development of the present computer code are 1) unstructured grid generation, 2) formulation of algebraic equations by implementing AUSM⁺-up on triangular mesh, 3) computations of boundary conditions at the solid and permeable walls, and 4) geometric modification with streamline model. These steps are detailed in the following sections.

A. Governing Equations

The continuity, momentum, and energy equations governing the unsteady two-dimensional flow of an inviscid fluid (normally referred as the Euler equations) are written in conservative form in the Cartesian coordinate system as follows:

$$\frac{\partial \mathbf{U}}{\partial t} + \frac{\partial \mathbf{F}}{\partial x} + \frac{\partial \mathbf{G}}{\partial y} = 0 \quad (1)$$

where

$$\begin{aligned}\mathbf{U} &= [\rho \quad \rho u \quad \rho v \quad \rho E]^T \\ \mathbf{F} &= [\rho u \quad \rho u^2 + p \quad \rho uv \quad \rho u H]^T \\ \mathbf{G} &= [\rho v \quad \rho uv \quad \rho v^2 + p \quad \rho v H]^T\end{aligned}$$

The above set of equations, when integrated over a control volume L with boundaries S with an outward normal l , gets transformed as

$$\frac{\partial}{\partial t} \iint_L \mathbf{U} d\Omega + \iint_{\Delta S} (\mathbf{F} l_x + \mathbf{G} l_y) dS = 0 \quad (2)$$

B. Implementation of AUSM⁺-Up on a Triangular Mesh

In the present work, a two-dimensional unstructured triangular mesh generator code is used to generate the initial triangular grids. A cubic-spline-fitting technique, with exponential stretching function to distribute the nodes more densely both at the leading edge and trailing edge, is used to discretize the boundary of the given domain. An envelope of equilateral triangles is formed around the wall boundary for the effective implementation of slip boundary condition. The entire cascade geometry is then Delaunay triangulated and the triangles are further refined by a node insertion method, wherein the locations of node insertion are selected among the circumcenter, Frey's point [16], and peer point based on the spacing test.

The output of the unstructured grid is written in the edge-based data structure. It consists of the node data, the edge data, and the cell topology data. The node data has information about node indices and their corresponding coordinates. The number of edges and the edge indices of the cell define the cell topology. Figure 2 shows a typical unstructured grid with triangular cells.

For the control volume cell L in a typical unstructured triangular grid of the computational domain pertaining to the subsonic compressor cascade, Eq. (2) can be rewritten in the ordinary differential form as

$$\left(\frac{d\mathbf{U}}{dt} \right)_L = - \frac{\Delta t}{\Omega_L} \left[\sum_{i=1}^{ne} (\mathbf{F}^i)_i \Delta S_i \right] \quad (3)$$

Although Eq. (3) is generic to any finite volume cell, be it in a structured or in an unstructured grid, the present algorithm is developed mainly for an unstructured (triangular) cell. Referring to Eq. (3) and Fig. 3, i indicates the edge of the cell L , ne is the total (3) number of edges in a (triangular) cell and ΔS_i is the length of the edge i .

The above ordinary differential equation is integrated using Euler's explicit formula to obtain the value of the solution vector for the new time step as

$$\mathbf{U}_L^{n+1} = \mathbf{U}_L^n - \frac{\Delta t}{\Omega_L} \left[\sum_{i=1}^{ne} (\mathbf{F}^i)_i \Delta S_i \right] \quad (4)$$

The conservative variable vector, $\mathbf{U}_L = [\rho \quad \rho u \quad \rho v \quad \rho E]^T$, is calculated at the cell center, and the convective flux vector,

$$\mathbf{F}_i^l = [(\rho V)_i \quad (\rho u V + l_x p)_i \quad (\rho v V + l_y p)_i \quad (\rho H V)_i]^T$$

is calculated at the edge i along the outward normal l for the time level n . The velocity component normal to the edge i is

$$V_i = (u l_x + v l_y) \quad (5)$$

The local time step Δt for a particular cell L is calculated using the Courant–Friedrichs–Lewy (CFL) condition for explicit solution methods given by

$$\Delta t = \left(\frac{\Delta D}{|V| + a|_L} \right) \cdot \text{CFL} \quad (6)$$

where ΔD is the length of the shortest edge of the cell L , and $|V|$ is the absolute velocity. As the present computations are time-marching, it is essential to ensure temporal accuracy in the scheme. The CFL number in the present scheme is maintained at 0.1, as higher values are found to yield an unstable behavior in the solution. The computation of the convective fluxes is accomplished by moving along the edges of the computational domain so that the repeated calculation of the values of fluxes crossing the same edge is avoided. Moreover, it also facilitates easy storage of the fluxes crossing all the edges.

The convective terms are considered as passive scalar quantities convected by the flow velocity at the interface and the pressure flux terms are governed by the acoustic speeds. At the edge i , the convective flux terms based on AUSM⁺-up algorithm are written as

$$\mathbf{F}_i^l = \boldsymbol{\psi}_i \cdot \mathbf{m}_i + \boldsymbol{\Pi}_i \cdot [0 \quad l_x \quad l_y \quad 0] \quad (7)$$

where $\boldsymbol{\psi}_i = [1 \quad u \quad v \quad H]^T$ and $\boldsymbol{\Pi}_i = [0 \quad p_i \quad p_i \quad 0]^T$

The mass flux at the interface is given by

$$\dot{m}_i = V_i \cdot \rho_{L/R} = a_i \cdot M_i \cdot \rho_{L/R} \quad (8)$$

where $\rho_{L/R}$ is the density is the interface density, dictated by the direction of V_i in accordance with idea of upwinding. Using Mach number as the working variable, the interfacial mass flux [Eq. (8)] can be written as

$$m_i = \begin{cases} a_i M_i \rho_L & \text{if } M_i > 0 \\ a_i M_i \rho_R & \text{otherwise} \end{cases} \quad (9)$$

The Mach number M_i is calculated as follows:

$$M_i = M^+(M)_L + M^-(M)_R - M_p \quad (10)$$

where

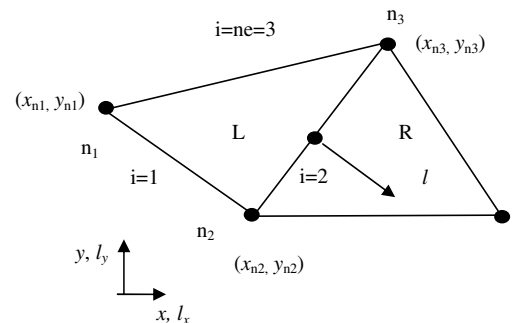


Fig. 3 Finite volume cell L , showing details of an edge with right neighbor R .

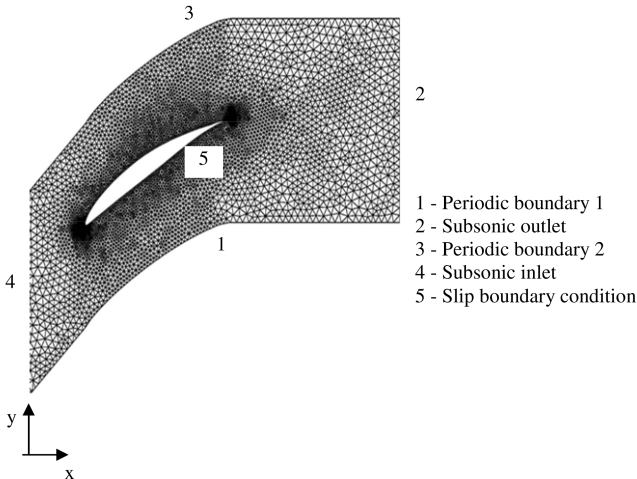


Fig. 2 Triangular grid in a subsonic compressor cascade.

$$M^\pm(M) = \begin{cases} \frac{1}{2}(M \pm |M|) & \frac{1}{2}(M \pm |M|) \\ \pm \frac{1}{4}(M \pm 1)^2 & (1 \mp 16\kappa(\pm \frac{1}{4}(M \pm 1)^2)) \end{cases} \quad (11)$$

A properly scaled pressure diffusion term that is used to enhance the calculation of low-Mach-number flow is defined as

$$M_p = \frac{K_p}{f_a} \max(1 - \sigma \tilde{M}^2, 0) \frac{(p_R - p_L)}{\rho_i a_i^2} \quad (12)$$

where

$$\rho_i = 0.5(\rho_L + \rho_R), \quad \tilde{M}^2 = \frac{(V_L^2 + V_R^2)}{2a_i^2}$$

where

$$a_i = 0.5(a_L + a_R), \quad V_{L/R} = u_{L/R} l_x + v_{L/R} l_y \\ f_a = M_0(2 - M_0), \quad M_0^2 = \min(1, \max(\tilde{M}^2, M_{co}^2))$$

In the above calculation, $\kappa = \frac{1}{8}$ and $K_p = 0.25$, and $\sigma = 1$. The cutoff Mach number M_{co} plays an important role in avoiding discontinuity in the pressure split functions and is kept as small as the characteristic value in the flow, which is the inlet freestream Mach number M_∞ in the present work.

In a simple upwind fashion, ψ_i is determined as

$$\psi_i = \begin{cases} \psi_L & \text{if } m_i > 0 \\ \psi_R & \text{otherwise} \end{cases}$$

The interface pressure is obtained from the pressure split functions as

$$p_i = p^+(M)_L p_L + p^-(M)_R p_R + p_u \quad (13)$$

where the pressure split functions are defined as

$$p^\pm(M) = \begin{cases} \frac{1}{2}(M \pm |M|)/M & \frac{1}{2}(M \pm |M|)/M \\ \pm \frac{1}{4}(M \pm 1)^2 & [(\pm 2 - M) \mp 16\zeta M(\frac{1}{4}(M \pm 1)^2)] \end{cases} \quad (14)$$

The velocity diffusion term that is inspired from characteristic relations is defined as

$$p_u = K_u p^+(M)_L p^-(M)_R (\rho_L + \rho_R) (f_a a_i) (u_R - u_L) \quad (15)$$

As suggested in [14], $K_u = 0.75$. To have a more suitable value of ζ for the all speed regimes, it is chosen as $\frac{3}{16}(-4 + 5f_a^2)$.

Second-order upwind spatial discretization is achieved by adopting the MUSCL approach [17] to an unstructured grid. Let us denote the vector of primitive variables as $\mathbf{q} = [\rho \ u \ v \ p]^T$. Higher-order accuracy is then achieved by expanding the cell-centered primitive variable to each cell edge i with a Taylor series:

$$\mathbf{q}_i = \mathbf{q}_{L/R} + \frac{\partial \mathbf{q}}{\partial x} \Big|_{L/R} (x_i - x_{L/R}) + \frac{\partial \mathbf{q}}{\partial y} \Big|_{L/R} (y_i - y_{L/R}) \quad (16)$$

$$\mathbf{q}_i = \mathbf{q}_{L/R} + \nabla \mathbf{q}_{L/R} \Delta \mathbf{r}_{L/R} \quad (17)$$

where $\nabla \mathbf{q}_{L/R}$ is the gradient defined at cell center L/R and $\Delta \mathbf{r}_{L/R}$ is the distance vector from left state L or right state R to i . Then based on [18], $\nabla \mathbf{q}_{L/R} \cdot \Delta \mathbf{r}_{L/R}$ is estimated as $\frac{1}{3}[\frac{1}{2}(q_{n2} + q_{n3}) - q_{n1}]$, and thus the primitive variable vector at the edge i is

$$\mathbf{q}_i = \mathbf{q}_{L/R} + \frac{1}{3}[\frac{1}{2}(q_{n2} + q_{n3}) - q_{n1}] \quad (18)$$

The values of nodal primitive variables \mathbf{q}_n are determined based on weighted average of the values at the center of cells c_{1-6} surrounding the node n , as shown in Fig. 4. Then

$$\mathbf{q}_n = \frac{\mathbf{q}_{c1}s_1 + \mathbf{q}_{c2}s_2 + \mathbf{q}_{c3}s_3 + \mathbf{q}_{c4}s_4 + \mathbf{q}_{c5}s_5 + \mathbf{q}_{c6}s_6}{s_1 + s_2 + s_3 + s_4 + s_5 + s_6} \quad (19)$$

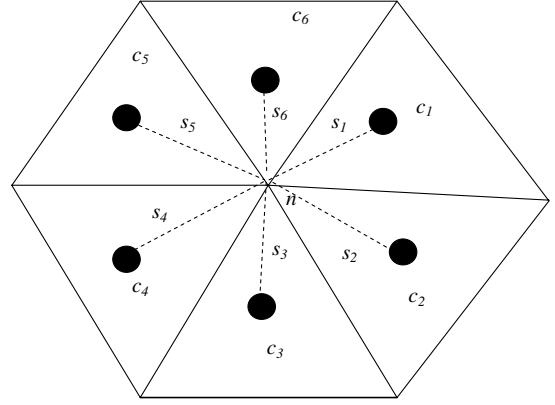


Fig. 4 Example of the cells shared by a node n .

where \mathbf{q}_c is the cell-centered primitive variable vector and s is the absolute distance of the cell center from the nodal point.

C. Boundary Conditions

1. Subsonic Inlet and Outlet

At the subsonic inlet, stagnation pressure P_{0i} , stagnation temperature T_{0i} , and inlet flow angle α_i are the prescribed boundary conditions. The Riemann invariant for interpolating speed of sound and the primitive variables are estimated following [19] at the inlet boundary i adjacent to the interior cell L (Fig. 3) as

$$R^- = u_L \cdot l_x + v_L \cdot l_y - \frac{2 \cdot a_L}{(\gamma - 1)} \quad (20)$$

$$K = \left\{ 1 + \cos \theta \sqrt{\frac{[(\gamma - 1)\cos^2 \theta + 2]a_0^2}{(\gamma - 1)(R^-)^2} - \frac{(\gamma - 1)}{2}} \right\} \quad (21)$$

$$a_i = \frac{-R^-(\gamma - 1)}{(\gamma - 1)\cos^2 \theta + 2} K \quad (22)$$

$$\cos \theta = \frac{-(u_L \cdot l_x + v_L \cdot l_y)}{\sqrt{(u_L)^2 + (v_L)^2}} \quad (23)$$

$$a_0^2 = a_L^2 + \frac{(\gamma - 1)}{2} (\sqrt{(u_L)^2 + (v_L)^2})^2 \quad (24)$$

$$T_i = T_{0i} \left(\frac{a_i^2}{a_0^2} \right) \quad (25)$$

$$p_i = p_{0i} \left(\frac{T_i}{T_{0i}} \right)^{\frac{\gamma}{\gamma - 1}} \quad (26)$$

$$\rho_i = \frac{p_i}{RT_i} \quad (27)$$

$$|V| = \sqrt{2 \cdot C_p (T_0 - T_i)} \quad (28)$$

$$u_i = |V| \cos \alpha_i \quad (29)$$

$$v_i = |V| \sin \alpha_i \quad (30)$$

At the outlet boundary, static pressure P_e is prescribed. The characteristic form of the 1-D Euler equations [18] normal to the boundary is used for estimating the other primitive variables:

$$p_i = p_e \quad (31)$$

$$\rho_i = \rho_L + \frac{(p_i - p_L)}{a_L^2} \quad (32)$$

$$u_i = u_L + l_x \frac{(p_L - p_i)}{\rho_L a_L} \quad (33)$$

$$v_i = v_L + l_y \frac{(p_L - p_i)}{\rho_L a_L} \quad (34)$$

2. Solid-Wall Boundary Condition

The values of boundary conditions are set for the primitive variables on the solid wall of the body according to the method of characteristics. Considering i (Fig. 3) as the boundary edge and L as the interior volume, these conditions are determined as follows:

$$p_i = p_L + \rho_L a_L (l_x u + l_y v) \quad (35)$$

$$\rho_i = \rho_L + (p_i - p_L)/a_L^2 \quad (36)$$

$$u_i = u_L - l_x (u \cdot l_x + v \cdot l_y)_L \quad (37)$$

$$v_i = v_L - l_y (u \cdot l_x + v \cdot l_y)_L \quad (38)$$

3. Permeable-Wall Boundary Condition

The static pressure is imposed on the blade wall during inverse calculations. Therefore, the velocity component normal to the wall need not be zero. The normal velocity on each boundary edge is calculated from the compatibility relation corresponding to eigenvalue $(V_n + a)_i$:

$$(V_n^{n+1})_i = (V_n^{n+1})_L - (\text{PPD}_i - p_L^{n+1})/(\rho a)_L^n \quad (39)$$

where p_L^{n+1} = CPD at the start of the time-marching iterative procedure, iter = 1. So,

$$(V_n^{n+1})_i = (V_n^{n+1})_L - (\text{PPD}_i - \text{CPD})/(\rho a)_L^n \quad (40)$$

assuming the eigenvalue to be always positive. If $(V_n^{n+1})_i$ is positive, first three compatibility relations allow for the computation of the other variables as shown below:

$$p_i^{n+1} = \text{PPD} \quad (41)$$

$$(V_t^{n+1})_i = (V_t^{n+1})_L \quad (42)$$

$$u_i^{n+1} = (V_n^{n+1})_i l_x + (V_t^{n+1})_i l_y \quad (43)$$

$$v_i^{n+1} = (V_n^{n+1})_i l_y - (V_t^{n+1})_i l_x \quad (44)$$

$$\rho_i^{n+1} = \rho_L^{n+1} + (p_i - p_L)^{n+1}/(a_i^n)^2 \quad (45)$$

If $(V_n^{n+1})_i$ is negative, two additional boundary conditions are required on total temperature $(T_0^n)_i$, and total pressure $(p_0^n)_i$, which are obtained from the previous time level. The remaining primitive variables on the boundary are calculated as follows:

$$p_i^{n+1} = \text{PPD} \quad (46)$$

$$T_i^{n+1} = (T_0^n)_i (p_i^{n+1}/p_0^n)^{(\gamma-1)/\gamma} \quad (47)$$

$$\rho_i^{n+1} = p_i^{n+1}/RT_i^{n+1} \quad (48)$$

$$(V)_i = \sqrt{2C_p(T_0^n - T_i^{n+1})} = \sqrt{(u_i^{n+1})^2 + (v_i^{n+1})^2} \quad (49)$$

$$(V_n^{n+1})_i = u_i^{n+1} l_y + v_i^{n+1} l_x \quad (50)$$

Solving the last two equations, we get u_i^{n+1} and v_i^{n+1} .

D. Modification of Geometry

After convergence of the inverse solver calculations, the pressure distribution on the blade is equal to the PPD distribution with nonzero normal velocity component on the blade permeable wall. This normal velocity along with the tangential velocity is used for defining the new blade shape:

$$\Delta n_q = \omega (V_n/V_t)_s \Delta s_{pq} \quad (51)$$

Referring to Fig. 5 and Eq. (51), Δn_q represents the modification vector at node q of the permeable-wall segment pq with unit normal vector l_{pq} (positive into the wall) and Δs_{pq} is the absolute elemental length between p and q along the blade surface. The modification vector is calculated at all points by moving along both suction and pressure surfaces separately starting from the stagnation point, where its value is zero.

The usage of the relaxation factor ω helps in avoiding the slope discontinuities of the resulting blade surface, particularly near the leading-edge region. As the relaxation factor value plays an important role in the number of design iterations, an optimum value should be chosen. In the present work, it is maintained as 0.5 in all the iterations. With the modification vector at all points calculated, the new blade coordinates are determined as follows:

$$x_q^{\text{ne}} = x_p^{\text{ne}} + (x_q^{\text{ol}} - x_p^{\text{ol}}) + \Delta n_q (l_{pq})_x \quad (52)$$

$$y_q^{\text{ne}} = y_p^{\text{ne}} + (y_q^{\text{ol}} - y_p^{\text{ol}}) + \Delta n_q (l_{pq})_y \quad (53)$$

where the superscripts ol and ne represent original (old) and final (new) coordinates of the blade profiles. The $(l_{pq})_x$ and $(l_{pq})_y$ are the values of the unit normal vector in the x and y directions, respectively. The blade surface is modified until the condition

$$\text{rms}[(\text{CPD} - \text{PPD})/p_0] \leq \varepsilon \quad (54)$$

is satisfied. In the present calculations, ε is chosen as 0.005.

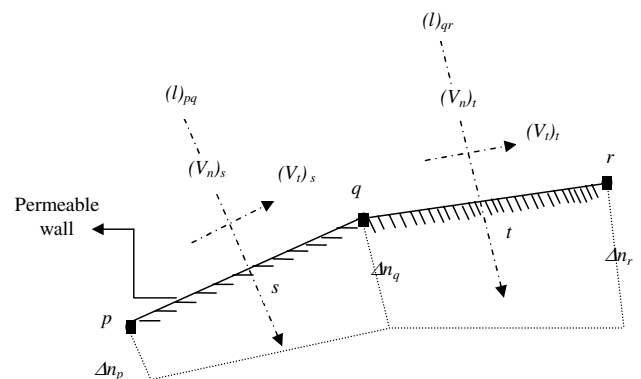
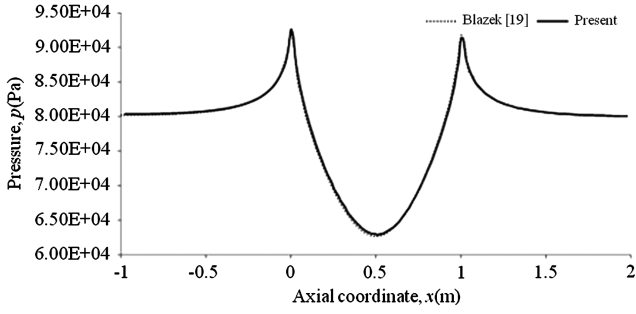
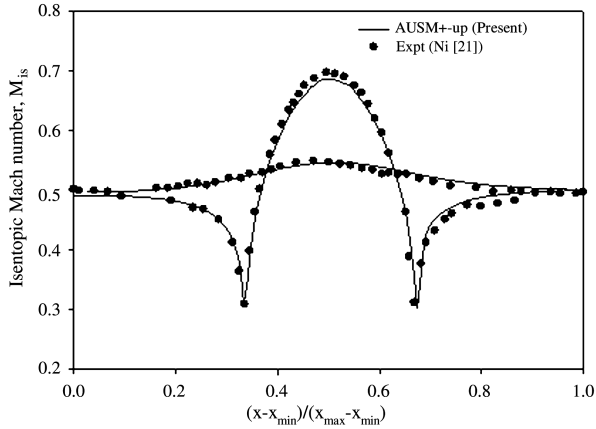


Fig. 5 Illustration of geometry modification.



a)



b)

Fig. 6 Plots of a) pressure distribution along the bottom surface of a channel having a 10% bump and b) distribution of isentropic Mach number in the channel having a circular bump at $M_{is,exit} = 0.5$.

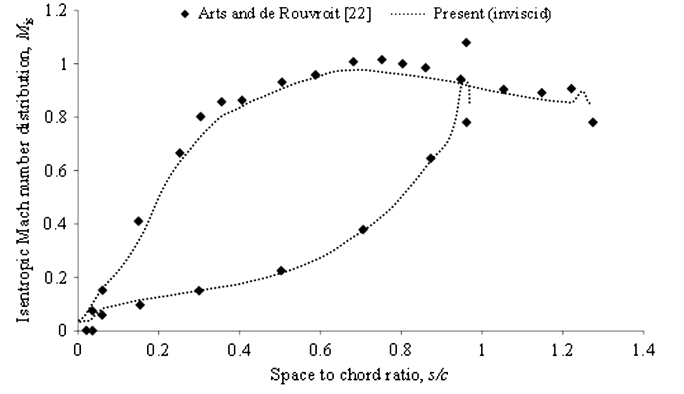


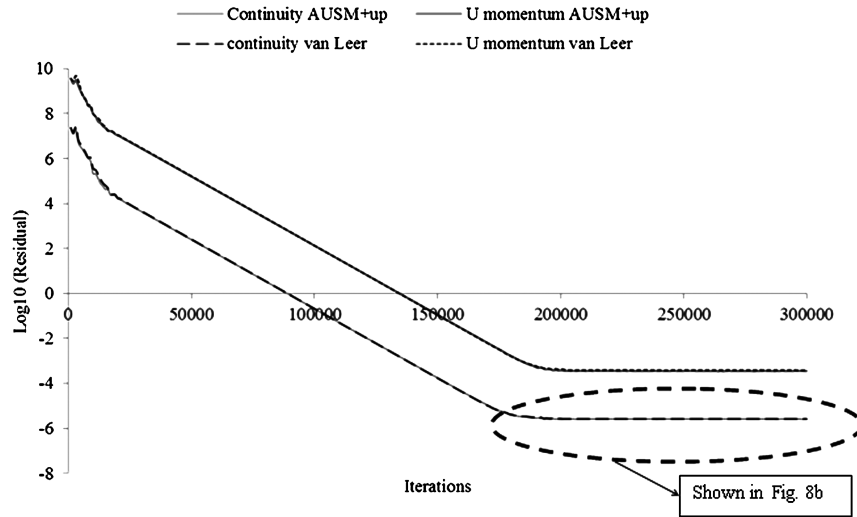
Fig. 7 Variation of isentropic Mach number over the surface of VKI LS-89 turbine inlet-guide-vane cascade.

E. Mesh Updates

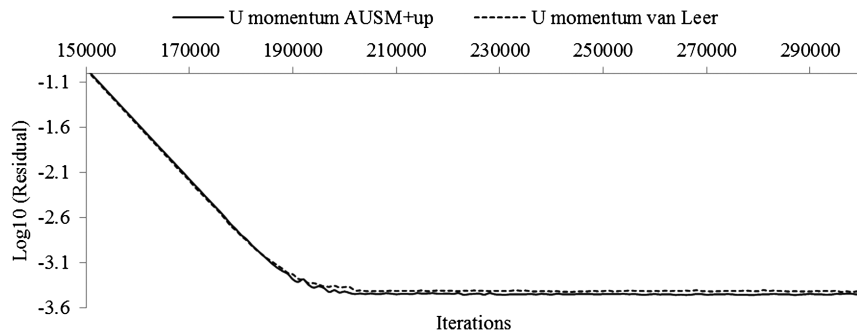
As the number of nodes on the pressure and suction sides of the blade is not equal and also they are not at the same x location of the blade, the segment spring analogy as discussed in [20] is used for the deformation of mesh for the modified blade geometry obtained in the previous step. The nodal segments are considered as springs that are taken as linear; therefore, when applied to the displacement of the springs, Hooke's law determines the force at every node p exerted by the surrounding node q ,

$$(F_p)_x = \sum_{q=1}^{nn} \zeta_{pq} (\delta_q - \delta_p)_x, \quad (F_p)_y = \sum_{q=1}^{nn} \zeta_{pq} (\delta_q - \delta_p)_y \quad (55)$$

where ζ_{pq} is the spring stiffness, $(F_p)_x$ and $(F_p)_y$ are the forces in x and y directions, ζ_q is the displacement of the surrounding node q , and nn is the total number of surrounding nodes.



a)



b)

Fig. 8 Convergence history for both van Leer and AUSM⁺-up flux-splitting schemes in the case of compressor cascade geometry.

At static equilibrium, force applied at every node p has to be zero. Then the iterative equation to be solved becomes

$$(\zeta_p^{k+1})_x = \frac{\sum_{q=1}^{nn} \zeta_{pq} (\delta_q^k)_x}{\sum_{q=1}^{nn} \zeta_{pq}}, \quad (\zeta_p^{k+1})_y = \frac{\sum_{q=1}^{nn} \zeta_{pq} (\delta_q^k)_y}{\sum_{q=1}^{nn} \zeta_{pq}} \quad (56)$$

The boundary conditions are of the Dirichlet type, given by known displacements δ of the boundaries. The displacement of blade profile is the difference between the new and old blade wall positions while that of the remaining boundaries (inlet, outlet and periodic) is maintained as zero throughout the calculation.

The spring stiffness ζ_{pq} is taken as proportional to the inverse of segment length

$$\zeta_{pq} = \frac{5}{\sqrt{(x_p - x_q)^2 + (y_p - y_q)^2}} \quad (57)$$

After solving Eq. (56) by Jacobi iteration, the nodes are displaced by adding the final displacement in both directions x and y as

$$x_p^{\text{new}} = x_p^{\text{old}} + (\delta_p^{\text{final}})_x \quad (58)$$

$$y_p^{\text{new}} = y_p^{\text{old}} + (\delta_p^{\text{final}})_y \quad (59)$$

Although the number of Jacobi iterations is generally fixed at less than 3000 [18], the value introduced in the present calculation is presented as 15,000 as an extreme.

III. Results

A. Validation of Direct Solver

1. Bump

The code developed for the Euler solver with the AUSM⁺-up scheme implemented on a triangular mesh is first validated for the problem of flow over a circular bump. The bump has a maximum thickness-to-chord ratio of 10% placed in the middle of the bottom wall of a channel. The computational domain extends to a distance of one chord length of bump in both the upstream and downstream sides of the bump. The ratio of stagnation pressure at the inlet to static

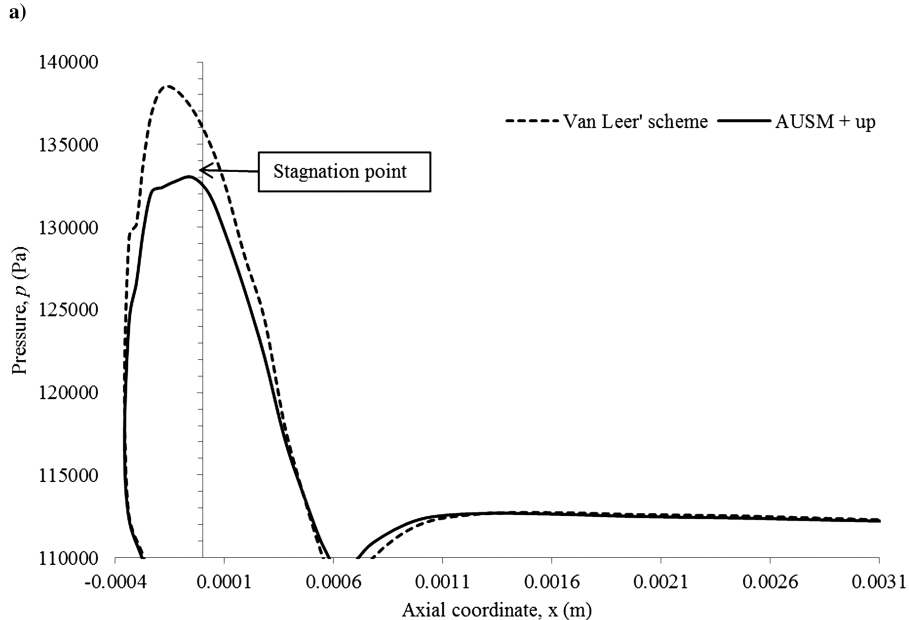
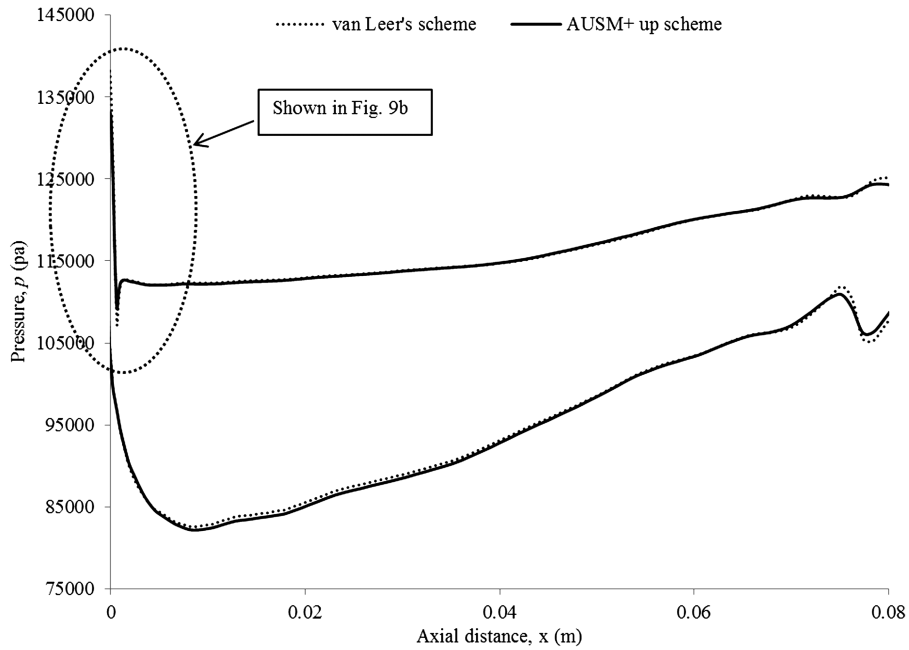


Fig. 9 Comparison of flux-splitting schemes for the compressor cascade geometry.

pressure at the exit (p_0/p) is taken as 1.25, which corresponds to an isentropic exit Mach number of 0.5731. In Fig. 6a, the pressure distribution along the bottom surface of the channel is compared with the results presented by Blazek [19], who used second-order-accurate central difference scheme with artificial dissipation. That the present computation yields such symmetric contours is indicative of the high accuracy levels of the scheme. In addition, the computational results are also compared with experimentally measured isentropic Mach number contours presented by Ni [21] for a different exit isentropic Mach number ($M_{is,exit} = 0.5$), and the results are shown in Fig. 6b.

2. VKI LS-89 Turbine Cascade Geometry

To validate the above Euler solver for a geometry with periodic boundaries, VKI LS-89 turbine inlet-guide-vane cascade geometry with blade stagger angle of 55 deg and space-to-chord ratio s/c of 0.85 is used. Figure 7 shows the isentropic Mach number distribution along the blade surface for an exit $M_{is} = 0.875$. The agreement between the present case and that of Arts and de Rouvoit [22] is very good for the above subsonic case, with a small discrepancy in the pressure-side trailing-edge region, which can be attributed to the absence of viscosity effects in the present calculation.

3. Comparison of AUSM⁺-up Scheme and Van Leer's Scheme

a. *Compressor Cascade Geometry (NACA 65-12a10)*. Figure 8 shows the convergence graph for the AUSM⁺-up and van Leer

schemes [15] for the inviscid calculation of NACA 65-12a10 compressor cascade geometry with space-to-chord ratio s/c of 1 and stagger angle $\beta = 31$ deg. For the sake of comparison of two different schemes, the first-order-accurate results are presented in the figure. The inlet stagnation pressure, stagnation temperature, and inlet flow angle are 133 kPa, 300 K, and 45 deg. The outlet static pressure is fixed as 117.3 kPa.

The static pressure distribution of the above compressor cascade geometry using van Leer's scheme, and AUSM⁺-up scheme is compared in Fig. 9. As it is observed, in the case of van Leer's scheme, the static pressure values in and around the stagnation-point region are more than the inlet stagnation pressure, which is impossible. As stated in the Introduction, such errors in the static pressure distribution at the leading-edge region are primarily due to the improper scaling of numerical dissipation term, particularly at the low-Mach-number regions. Since the inverse design algorithm starts from the stagnation-point region, the errors percolate to the geometry modification. Because of the criticality of the leading-edge region in the blade modification step, usage of AUSM⁺-up enhances the accuracy of inverse design calculation. This will be demonstrated in the next section.

b. *Turbine Cascade Geometry (VKI LS-89)*. In the same vein, the static pressure distribution of the turbine cascade geometry of VKI LS-89 (used for validation) using van Leer's scheme and AUSM⁺-up scheme is compared in Fig. 10. The inlet stagnation pressure, stagnation temperature, and flow angle are 166.83 kPa, 420 K, and 0 deg. The outlet static pressure is fixed as 1 kPa. Similar

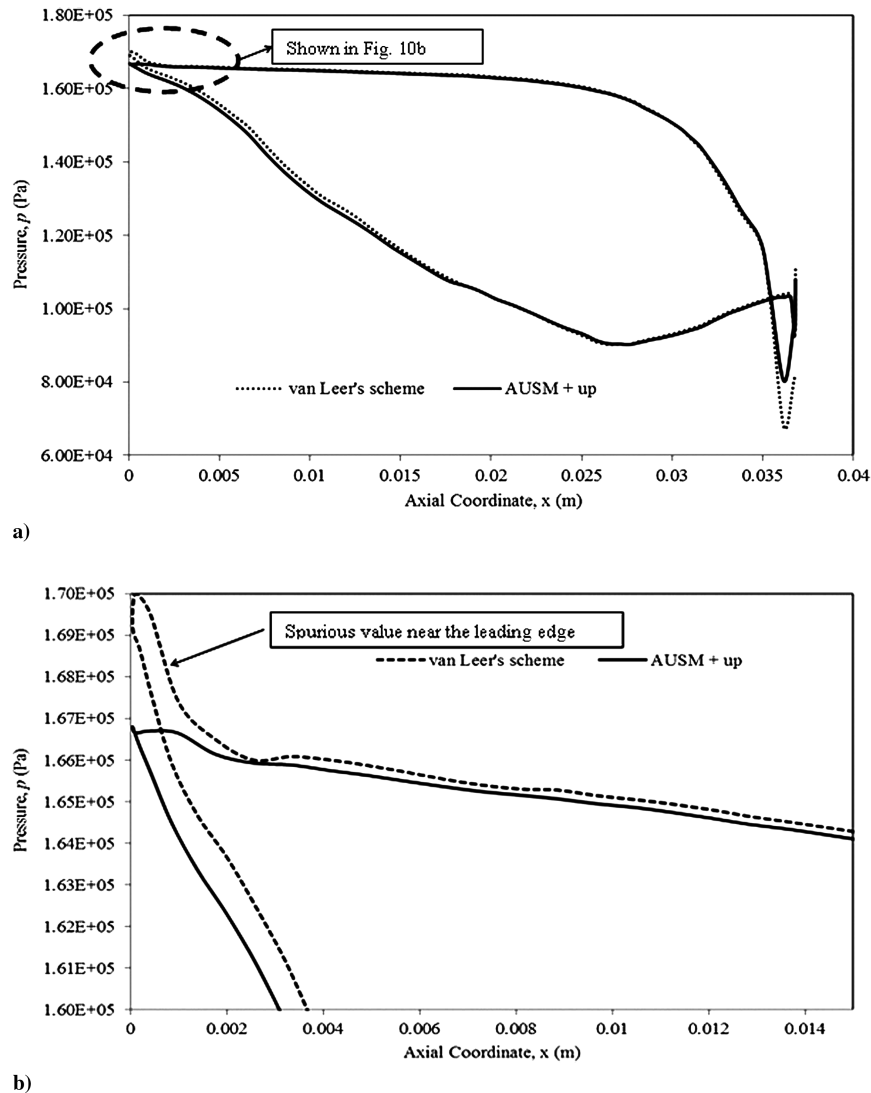


Fig. 10 Comparison of flux-splitting schemes for the turbine cascade geometry.

Table 1 Error comparison for the blade profiles obtained from inverse codes using AUSM⁺-up and van Leer scheme for flux calculation

	Pressure distribution p/p_0	
	Maximum error, %	RMS error, %
Van Leer's scheme	7.8	1.4
AUSM ⁺ -up scheme 10,875 (coarse)	3.0	0.5
AUSM ⁺ -up scheme 16,016 (medium)	2.49	0.42
AUSM ⁺ -up scheme 24,967 (fine)	2.31	0.35

to compressor cascade results, the spurious errors in the prediction of static pressure distribution at the leading edge observed in the case of van Leer's scheme, due to the excessive numerical dissipation errors and improper scaling of speed of sound were removed in the AUSM⁺-up scheme.

B. Results from Inverse Design

To begin with, a comparison of inverse design results between van Leer's and AUSM⁺-up scheme for compressor cascade geometry is performed. The initial guess is taken as NACA 65-12a10 ($\beta = 31$ deg, $s/c = 1$) compressor blade geometry, and the required blade profiles are another family of compressor cascade geometry, NACA 65-12a2i8b ($\beta = 31$ deg, $s/c = 1$). The results are

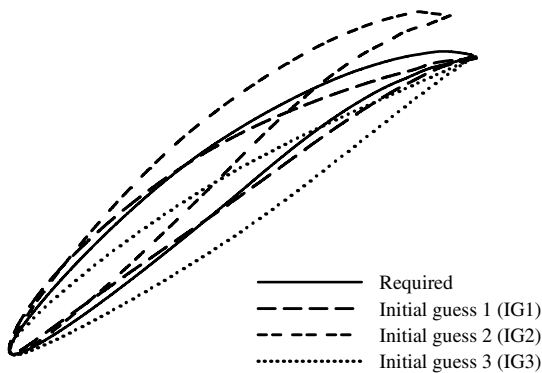


Fig. 11 Comparison of initially guessed and required blade profiles.

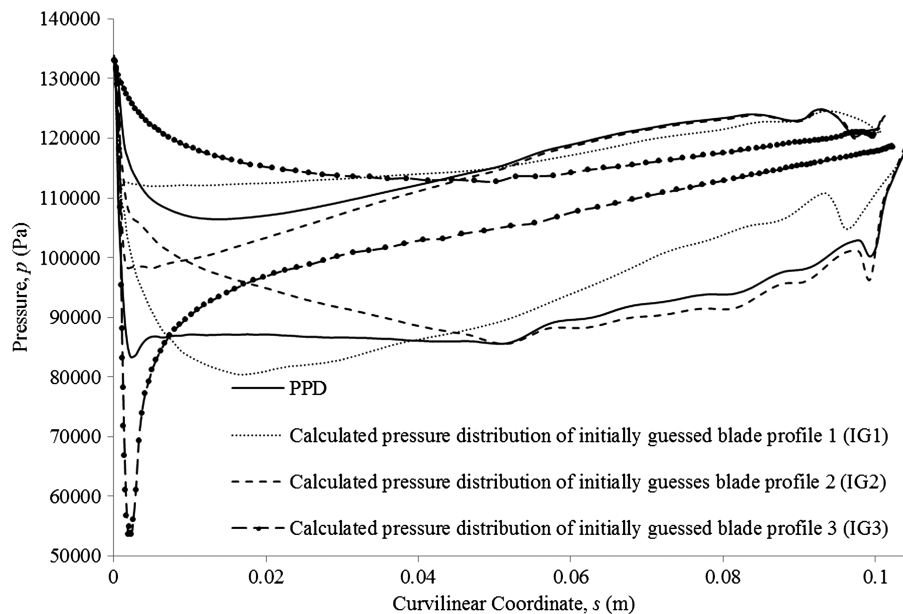


Fig. 12 Prescribed pressure and pressure distributions of initially guessed blade profiles (IG1, IG2, and IG3).

summarized in Table 1, and thus it can be seen that the maximum and rms values of the errors both in pressure values and absolute coordinate values decrease with the usage of AUSM⁺-up in the inverse design algorithm. Further, a grid refinement study is conducted with 10,875 (coarse), 16,016 (medium), and 24,967 (fine) mesh cells. It has been found that the maximum as well as rms errors significantly reduced with the refined mesh.

Secondly, to find the effect of initial guesses on the final results, the inverse design is performed to obtain a known blade profile starting from three different initial guesses separately to check the independence of the methodology on the initial condition. The initially guessed blade profile 1 (IG1) is a NACA 65-12a10 compressor blade with cascade geometry parameters, stagger angle $\beta = 31$ deg, and space-to-chord ratio of $s/c = 1$. The initially guessed blade profile 2 (IG2) is a NACA 65-12a2i8b compressor blade with cascade geometry parameters stagger angle $\beta = 36$ deg and space-to-chord ratio of $s/c = 1$. The third initial guess is the NACA 65-210 with stagger angle $\beta = 31$ deg and space-to-chord ratio of $s/c = 1$. The required blade profile is a NACA 65-12a2i8b compressor blade profile with cascade geometry parameters, stagger angle $\beta = 31$ deg, and space-to-chord ratio of $s/c = 1$. The boundary conditions are maintained the same for all the cases as $p_0 = 133$ kPa, $T_0 = 330$ K, $p = 117.3$ kPa, and $\alpha = 45$ deg so that the flow is subsonic. The IG1 cascade geometry is discretized with 10,875 triangular cells with 227 nodal points distributed around the blade profile while the IG2 cascade geometry is discretized with 11,749 triangular cells with 180 nodal points distributed around the blade profile.

The pressure distribution corresponding to the required geometry (PPD) and initial blade geometries IG1, IG2, and IG3 (Fig. 11) are plotted against the curvilinear coordinate, s (in meters) in Fig. 12. A significant difference in loading between the required and initial pressure distribution can be observed in both the cases. After eight design iterations (iter = 8) for the inverse design starting from IG1 geometry, nine design iterations (iter = 9) for the inverse design starting from IG2 geometry and 13 design iterations (iter = 13) for that starting from IG3 geometry, the pressure distribution for the final blade shapes are shown in Fig. 13. The corresponding final blade shapes are shown in Fig. 14. The number of iterations taken is directly proportional to the loading difference between the required and pressure distribution. Hence, it can be reduced considerably if the initial geometry is guessed so that it is close to the required profile. That final blade shapes of the inverse design process starting from three different initial guesses are close to the required blade profile proves that the robustness of the inverse algorithm. The problem of trailing-edge closure is solved by rotating the blades

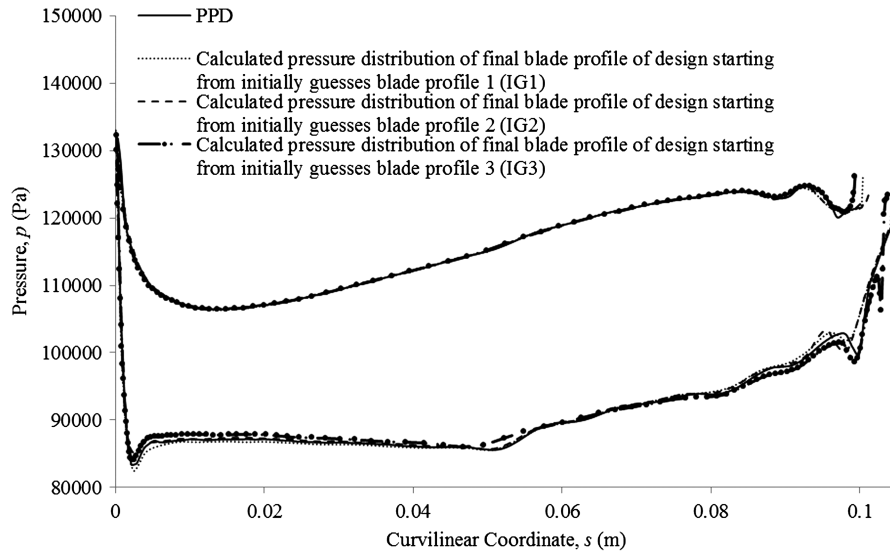


Fig. 13 Prescribed pressure and calculated pressure distributions of final geometry obtained from inverse design starting with initially guessed blade profiles (IG1, IG2, and IG3).

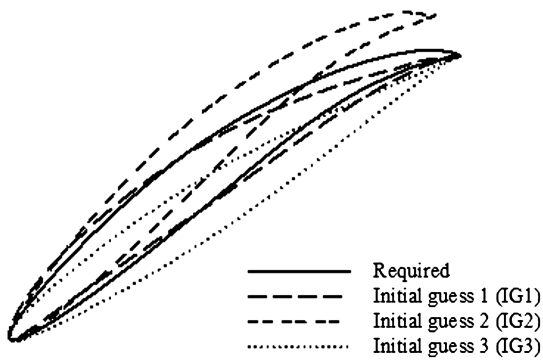


Fig. 14 Comparison of final and required blade profiles.

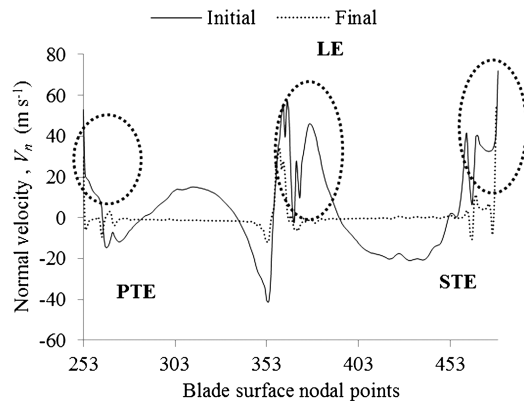


Fig. 15 Normal velocity distribution on the blade surface in IS of the design starting with IG1.

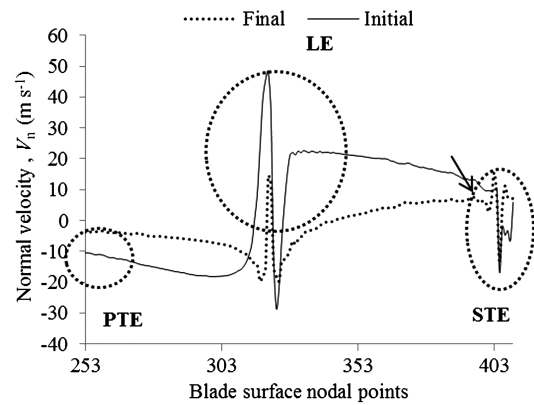


Fig. 16 Normal velocity distribution on the blade surface in IS of the design starting with IG2.

around the leading edge to maintain a constant trailing-edge thickness.

As the above inverse methodology is dependent on the normal velocity on the blade surface (obtained after the steady-state convergence of the inverse solver), which is again a function of difference in CPD and PPD [Eq. (39)], the decrease in the above distribution in the inverse solver can be considered as an exact measure of the convergence. Figure 15 shows the normal velocity plotted against the blade nodal locations [starting from the pressure-side trailing edge (PTE) to the suction-side trailing edge (STE)], both at the beginning and at the end of design iteration in the IS for the design starting from IG1. It is seen that the normal velocity distribution is found to decrease drastically from the first to the eighth design iteration. Larger values at the leading-edge (LE) and

Table 2 Comparison of flow parameters for different initial guesses IG1, IG2, and IG3 for the design of NACA 65-12a2i8b

Parameter	Required	Initial	Initial % difference	Obtained	Final % difference
Mass flow rate, kg s^{-1}					
IG1	18.109	17.909	1.104	18.11	0.005
IG2	18.109	17.517	3.265	18.096	0.06
IG3	18.109	16.38	9.5	18.094	0.08
Flow angle at exit, deg					
IG1	18.012	20.629	14.529	18.10	0.4885
IG2	18.012	23.188	28.73	18.19	0.9882
IG3	18.012	30.97	41.84	18.30	1.5

trailing-edge regions (PTE and STE) can be attributed to the numerical errors already present in the direct solver computation using solid-wall boundary condition. Similarly, Fig. 16 shows the trend in normal velocity distribution in the IS for the inverse design process starting from initially guessed geometry (IG2).

Table 2 gives information regarding the variation in mass flow rate during the design process starting with initial guesses IG1 and IG2. The initial percentage difference in mass flow rate and flow angle for IG1 is found to be 1% and that of exit flow angle is 14.60%. This error reduces to 0.005% for mass flow rate and to 0.48% for the flow angle at the end of inverse design process. Similar comparison is made for the inverse design starting with IG2 and IG3 as initial guesses and is detailed in Table 2.

IV. Conclusions

AUSM⁺-up scheme is implemented on an unstructured grid for an iterative inverse design procedure. The scheme for flux computation shows better accuracy in comparison with the other flux-splitting schemes, especially in the leading-edge region of airfoils in a compressor cascade. The robustness of the inverse design method is demonstrated by obtaining the same final blade profile for a prescribed pressure distribution, even with three different initial guesses. Although the number of iterations depends to some extent on the initial guess, the number as such is not very significant. The main advantage is that a relatively inexperienced designer can obtain blade profiles of desired pressure distribution with relative ease. The computer algorithm proposed in this paper can be used to develop an effective inverse design code for turbomachinery applications.

References

- [1] Demeulenaere, A., and van den Braembussche, R., "Three-Dimensional Inverse Method for Turbomachinery Blading Design," *Journal of Turbomachinery*, Vol. 120, 1998, pp. 247–255. doi:10.1115/1.2841399
- [2] Demeulenaere, A., Leonard, O., and van den Braembussche, R., "A Two-Dimensional Navier Stokes Inverse Solver for Compressor and Turbine Design," *Proceedings of the Institution of Mechanical Engineers Part A, Power and Process Engineering*, Vol. 211, 1997, pp. 299–307.
- [3] Leonard, O., and van den Braembussche, R., "Design Method for Subsonic and Transonic Cascade with Prescribed Mach Number Distribution," *Journal of Turbomachinery*, Vol. 114, 1992, pp. 553–560. doi:10.1115/1.2929179
- [4] Daneshkhah, K., and Ghaly, W. S., "An Inverse Blade Design Method for Subsonic and Transonic Viscous Flow in Compressors and Turbines," *Inverse Problems in Science and Engineering*, Vol. 14, 2006, pp. 211–231. doi:10.1080/17415970500354235
- [5] Tiow, W. T., Yiu, K. F. C., and Zangeneh, M., "Application of Simulated Annealing to Inverse Design of Transonic Turbomachinery Cascades," *Proceedings of the Institution of Mechanical Engineers Part A, Power and Process Engineering*, Vol. 216, 2002, pp. 59–73.
- [6] Tiow, W. T., and Zangeneh, M., "Application of a Three Dimensional Viscous Transonic Inverse Method to NASA Rotor 67," *Proceedings of the Institution of Mechanical Engineers Part A, Power and Process Engineering*, Vol. 216, 2002, pp. 243–255. doi:10.1243/095765002320183568
- [7] Ahmadi, M., and Ghaly, W. S., "Aerodynamic Design of Turbomachinery Cascades Using a Finite Volume Method on Unstructured Meshes," *Proceedings of the 5th Conference of CFD Society of Canada (CFD-97)*, 1997, pp. 2.15–2.21.
- [8] Dang, T., "Euler-Based Inverse Method for Turbomachine Blades Part 1: Two-Dimensional Cascades," *AIAA Journal*, Vol. 33, No. 12, 1995, pp. 2309–2315. doi:10.2514/3.12985
- [9] Choo, M. F., and Zangeneh, M., "Development of an (Adaptive) Unstructured 2-D Inverse Design Method for Turbomachinery Blades," *ASME Turbo Expo*, ASME International, New York, 2002.
- [10] Lee, D., "Local Preconditioning of the Euler and Navier-Stokes Equations," Ph.D. Dissertation, Aerospace Engineering, University of Michigan, Ann Arbor, MI, 1996.
- [11] Liou, M.-S., "Ten Years in the Making—AUSM-Family," NASA/TM-2001-21077.
- [12] Liou, M.-S., and Edwards, J. R., "Numerical Speed of Sound and Its Application to Schemes for All Speeds," NASA TM-1999-209286.
- [13] Weiss, J. M., and Smith, W. A., "Preconditioning Applied to Variable and Constant Density Time-Accurate Flows on Unstructured Flows on Unstructured Meshes," *AIAA Paper 94-2209*, 1994.
- [14] Liou, M.-S., "A Sequel to AUSM, Part II: AUSM⁺-Up for All speeds," *Journal of Computational Physics*, Vol. 214, 2006, pp. 137–170. doi:10.1016/j.jcp.2005.09.020
- [15] Nair, P., Jeyachandran, T., Puranik, B., and Bhandarkar, U. V., "Simulation of Thermo Fluid Interactions in Cryogenic Stage Turbine Startup System Using AUSM⁺-Up Based Higher Order Accurate Flow Solver," *Defence Science Journal*, Vol. 39, No. 3, 2009, pp. 215–229.
- [16] Frey, W. H., "Selective Refinement: A New Strategy for Automatic Node Placement in Graded Triangular Meshes," *International Journal for Numerical Methods in Engineering*, Vol. 24, 1987, pp. 2183–2200. doi:10.1002/nme.1620241111
- [17] van Leer, B., "Towards the Ultimate Conservative Difference Scheme V. A Second Order Sequel to Godunov's Method," *Journal of Computational Physics*, Vol. 32, 1979, pp. 174–206. doi:10.1016/0021-9991(79)90145-1
- [18] Frink, N. T., "A Fast Upwind Solver of the Euler Equations on a three-Dimensional Unstructured Meshes," *AIAA Paper 91-0102*, 1991.
- [19] Blazek, J., *Computational Fluid Dynamics: Principles and Applications*, 1st ed., Elsevier, Oxford, 2001.
- [20] Blom, F. J., "Considerations on the Spring Analogy," *International Journal for Numerical Methods in Fluids*, Vol. 32, 2000, pp. 647–668. doi:10.1002/(SICI)1097-0363(20000330)32:6<647::AID-FLD979>3.0.CO;2-K
- [21] Ni, R. H., "A Multiple-Grid Scheme for Solving the Euler Equations," *AIAA Journal*, Vol. 20, 1982, pp. 1565–1571. doi:10.2514/3.51220
- [22] Arts, T., and de Rouvoit, M. L., "Aero Thermal Performance of a Two-Dimensional Highly Loaded Transonic Turbine Nozzle Guide Vane: A Test Case for Inviscid and Viscous Flow Computations," *Journal of Turbomachinery*, Vol. 114, 1992, pp. 286–289. doi:10.1115/1.2927978

J. Oefelein
Associate Editor